This is the accepted manuscript made available via CHORUS. The article has been published as:

Role of magnetism on transition metal oxide surfaces in vacuum and solvent

V. S. Chaitanya Kolluru and Richard G. Hennig

Phys. Rev. Materials **4**, 045803 — Published 16 April 2020

DOI: 10.1103/PhysRevMaterials.4.045803

Role of magnetism on transition metal oxide surfaces in vacuum and solvent

V. S. Chaitanya Kolluru and Richard G. Hennig*
Department of Materials Science and Engineering,
University of Florida, Gainesville, FL 32611, U.S.A.
(Dated: February 19, 2020)

The transition metal oxides MnO, FeO, NiO, and CoO are essential materials systems for catalysis applications and energy technologies. These materials exhibit a magnetic phase transition from paramagnetism to antiferromagnetism upon cooling. In this work, we show that an accurate treatment of the surfaces requires a description of the disordered local magnetic moments of the paramagnetic phase. We determine how the magnetic phase transition and the presence of solvent affect the surface energies using density-functional theory and a solvation model. To accurately account for the correlations in the *d*-electron system, and to match the observed magnetic order and bandgaps of the room temperature phases, we include the Hubbard-*U* correction. In the case of MnO, FeO, and CoO, which are paramagnetic semiconductors or insulators at room temperature, we demonstrate the importance of the local magnetic moments and model the materials using special quasirandom structures. To determine the equilibrium shape of MnO, FeO, NiO, and CoO nanocrystals, we calculate the surface energies of their low-energy (100), (110), and (111) facets and perform the Wulff construction. For the (111) facet, we consider various reconstructions that remove the polar nature of the unreconstructed surface. The processing conditions of these oxide nanoparticles, in most cases, involves a solvent. To analyze the influence of the solvent environment on the surface energies of different facets and thereby the crystal shape, we calculate the surface energies of these oxides in water using the continuum solvation model VASPsol. We find that the surface energies decrease due to the dielectric screening. However, as the ratio of surface energies remains sufficiently similar, we predict that the equilibrium crystal shape is only weakly affected by the presence of the solvent.

I. INTRODUCTION

The rocksalt structured transition metal monoxides (TMOs) – MnO, FeO, CoO, and NiO – are of great interest due to their diverse physical properties and have a broad range of applications in catalysis [1, 2], electronics [3], electrochemical energy storage [4, 5], and others [6]. At low temperatures, they are all antiferromagnetic insulators with large bandgaps. At room temperature, MnO, FeO, and CoO are paramagnetic insulators. The strong localization of *d*-electrons and the magnetic behavior of these materials pose a challenge for an accurate description of the properties of these systems in computational methods, such as density functional theory.

The electronic structure of the TMOs is sensitive to magnetic ordering. At low temperatures, all four oxides, MnO, FeO, CoO, and NiO, display an antiferromagnetic type II (AF-II) magnetic ordering, where up and down spins order in (111) layers that alternate along the [111] direction [7]. The AF-II ordering is responsible for the insulating nature of these monoxides, whereas ferromagnetic and non-spinpolarized calculations wrongly predict metallic behavior [8, 9]. The AF-II ordering is associated with a structural distortion. Below the Néel temperature, the cubic structure displays a rhombohedral distortion for MnO and NiO [10–12] and a monoclinic distortion for FeO and CoO [7, 13–15]. The Néel temperatures are 116 K (MnO), 198 K (FeO), 291 K (CoO), and 525 K (NiO) [16]. For MnO, FeO, and CoO, the Néel temperature is below room temperature, and hence these oxides exist in a paramagnetic state at ambient conditions.

The surfaces of these rocksalt oxides are actively studied by both theoretical [17] and experimental methods [18]. The (111) surfaces of MnO [19], FeO [20–25], CoO [25–27], and NiO [25, 28–38] received particular attention due to their polar nature and reactivity [39, 40] and are all extensively studied to understand their surface structure and properties. Previous studies suggest that the (111) octopolar reconstruction is the most stable reconstruction for NiO(111) [35]. The octopolar reconstructed (111) surface consists of three-faceted (100) pyramids or islands on the surface. The CoO(111) surface forms a Co_3O_4 layer in oxygen-rich conditions and otherwise adsorbs oxygen or hydroxyl groups that passivate the surface and prevent reconstruction [25]. The FeO(111) surface forms a Fe_3O_4 layer under oxygen-rich conditions [25, 41, 42], and under iron-rich conditions the surface reconstructs [25]. The MnO(111) surface shows an octopolar reconstruction [43] or can get stabilized by adsorption of OH groups [44, 45]. Given the several applications [1–6] and interest in the these oxide surfaces, there is a need to accurately describe the Hamiltonian for the room temperature phases of these oxides.

While there are many studies of the structure of the oxide surfaces, little is known about the role of magnetism and solvation on the surface structure and energies. Surface energies are difficult to measure and furthermore affected by the presence of solvent, adsorbates, defects, and impurities. First-principles approaches can provide in-

* rhennig@ufl.edu

sight into the surface energies and the relative stability of oxide surfaces.

In this work, we determine the effect of the paramagnetic and antiferromagnetic state on the surface energy of the rocksalt TMOs, MnO, FeO, CoO, and NiO, using density-functional theory (DFT). Since the magnetic ordering affects the electronic and other properties, we aim to describe the room-temperature paramagnetic state for MnO, FeO, and CoO, and the antiferromagnetic state for NiO.

We start with a validation of the accuracy of our DFT methodology for the electronic and magnetic structure of the oxides. To correctly describe the energy and electronic structure of the antiferromagnetic ground state of these oxides requires a description of the d-electron correlations for which we employ the Hubbard-U correction. We find that an accurate description of the paramagnetic state for MnO, FeO, and CoO at ambient condition requires an explicit description of the disordered local moments as non-spinpolarized calculations result in unphysically high energies and incorrect bandgaps. We describe the disordered local moments through special quasirandom structures (SQS) in a sufficiently large supercell. Trimarchi *et al.*, recently showed that supercells employing SQS structures of local disordered moments can capture the experimentally observed insulating behavior of the paramagnetic transition metal oxides [46].

Based on this description of the magnetic and electronic structure, we determine the surface energies and predict the shape of the nanocrystals. Our calculations predict a cube crystal shape for all four oxides. For MnO, the surface energies remain nearly the same across the magnetic transition, while for FeO and CoO, the surface energy is, in fact, lower in the high-temperature paramagnetic state. Finally, we observe that dielectric screening of the crystalline surfaces in water described by the solvation model VASPsol [47, 48] slightly lowers the surface energies but only weakly affects the crystal shapes. This work provides a methodology to estimate the surface properties of TMOs using a validated DFT description of magnetic ordering and structure.

II. METHODS

A. Density-functional calculations

We perform DFT calculations using the projector-augmented wave method as implemented in the Vienna Ab-initio Simulation Package (VASP) [49–51]. For the exchange-correlation functional we employ the Perdew-Burke-Ernzerhof (PBE) approximation [52]. For the choice of PAW potential, we follow the suggestion of the Materials Project [53, 54] and include for Mn, Fe, and Ni the $3p$ electrons as valence electrons. To account for the electronic correlation of the d orbitals and correct the underestimate of the bandgap and unphysical negative surface energies of the PBE functional, we apply the Hubbard-U correction for all four transition metal oxides with the values of U for each of the four transition metals (TM) taken from MaterialsProject [54, 55]. **The U values are provided in Tab. III. Previous work suggests that NiO has both Mott-Hubbard and charge transfer type character leading to the band gap [56]. Future calculations with computationally more demanding hybrid functionals such as the HSE06 functional could improve the description of the hybridization between the Ni d and O p states along with the correlation between the Ni d orbitals.** To ensure an accuracy of the energies of 1 meV/atom and of the surface energies of better than 1 meV/Å^2 we use a plane-wave basis cutoff energy of 450 and 600 eV for vacuum and solvent calculations, respectively, and k-point meshes with a density of 30 per Å^{-1}. A higher cutoff energy is required for solvent calculations to ensure sufficient resolution for the interfacial region. For the structural relaxations, we find an improved convergence using the quasi-Newton method compared to the conjugate gradient method.

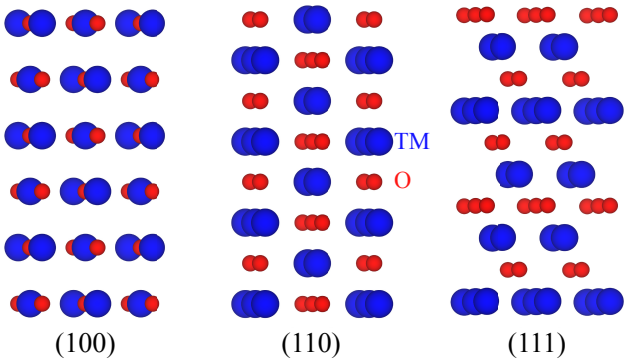

FIG. 1. (Color online) Side views of the (100), (110), and unreconstructed polar (111) surface slabs of the transition metal oxide systems.

B. Surface structures

We create slabs of the (100), (110), and (111) facets of the four TMOs with the MPInterfaces package [57], as illustrated in Fig. 1. For each slab, the structure of the top and bottom layers is equivalent, leading to equal contributions to the surface energy from both surfaces. We relax the positions of the atoms in the two outermost layers at the top and bottom surface while keeping the remaining atoms in the center of the slab fixed and constrain the in-plane lattice parameters to the relaxed bulk values. To determine the effect of the slab thickness on the surface energy, we perform calculations for slabs containing 5 to 12 layers of atoms, corresponding to a thickness of 8 to 20 Å, and extrapolate to infinite slab thickness (see Sec. III E). We find that to converge the

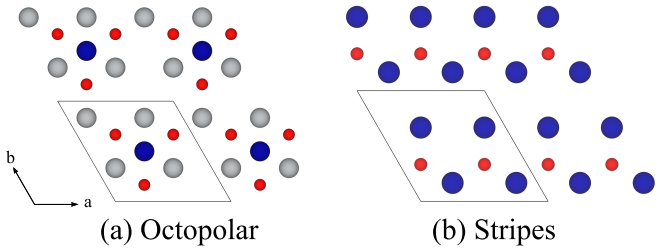

FIG. 2. (Color online) (a) Top view of the top three layers of a metal terminated octopolar (oct-M) reconstruction. A pyramid of M_1-O_3-M_4 (Blue-Red-Grey) is formed on the surface. (b) Top view of the oxygen terminated stripes reconstruction (stripes-O), which has alternate rows of the oxygen in the top-most layer removed.

energies of the slabs to 1 meV/atom and the surface energies to better than 1 meV/Å^2 requires a vacuum spacing of at least 6 Å. To further reduce the interactions between the slabs, we set the vacuum spacing for all calculations to 15 Å.

The (111) surfaces of the rocksalt structure for ionic materials are polar and highly unstable [58]. We follow the work on surface reconstructions of MnO(111) by Franchini *et al.* [19], and select two types of stoichiometric and charge-neutral reconstructions – octopolar and stripes – for each oxide with metal or oxygen terminations. Figure 2(a) shows the octopolar reconstruction, consisting of islands of either metal or oxygen atoms where 3/4 of the atoms in the top layer and 1/4 of the atoms in the second layer are removed. Figure 2(b) illustrates the stripes reconstruction that removes alternating parallel rows of either metal or oxygen atoms in the top surface layer. We first calculate the energies for each reconstruction for a similar bulk thickness to determine the most favorable reconstruction for each system. Then we construct slabs of thicknesses ranging from 14 to 20 Å for the energetically most favorable reconstruction and extrapolate the surface energy to infinite slab thickness.

C. Solvation calculations

The synthesis and applications of the nanocrystals of these oxides often involve solvents and electrolytes [2]. To determine the effect of water on the surface energies and shapes of TMO nanocrystals, we calculate the solvation energy of the surfaces using the continuum solvation model VASPsol [47, 48]. Similar to the vacuum case, we perform calculations for different thicknesses of slabs for the (100), (110), and the stable reconstructed (111) facets for each system in water. We determine the shape of the transition metal nanocrystals in vacuum and water using the Wulff construction with the MPInterfaces package [57]. **The implicit solvation model considers the electrostatics, cavitation, and dispersion effects of the dielectric solvent. However, to study the chemical aspects of solvation on surfaces, more expensive calculations with explicit layers of water molecules should be performed. Such a study could also determine the effect of the applied electric potential on the surface structure, adsorbed hydrogen and hydroxyl ions, and surface energies [48].**

TABLE I. Comparison of the rhombohedral distortions ($R\bar{3}m$) for the relaxed AF-II structures of MnO and NiO with previous DFT calculations and experimental work. The rhombohedral distortion angle is $\Delta\alpha = \alpha - 90°$ and V is the volume per formula unit. **This work and Ref. [59] use the PBE functional with Hubbard-U correction. The U values are reported in Table III. Ref. [59] used $U = 4$ eV for all oxides.**

		$\Delta\alpha$ (deg.)	V(Å^3)
MnO	DFT (this work)	0.77	22.66
	DFT [59]	0.72	22.6
	Exp. [7, 11, 12, 60]	0.43 - 0.62	21.7 - 21.8
NiO	DFT (this work)	0.05	18.76
	DFT [59]	0.07	18.5
	Exp. [10, 11, 61]	0.08 - 0.1	18.1 - 18.2

TABLE II. Comparison of the monoclinic distortions ($C2/m$) for the relaxed AF-II structures of FeO and CoO with prior DFT calculations and experimental work. The monoclinic distortion angle is $\Delta\beta = \beta - 125.264°$, a', b', and c' are the lattice constants of the pseudo-orthorhombic lattice constants as defined by Schrön *et al.* [59], and V is the volume per formula unit. **This work and Ref. [59] use the PBE functional with Hubbard-U correction. The U values are reported in Table III. Ref. [59] used $U = 4$ eV for all oxides.**

		$\Delta\beta$ (deg.)	c'/a'	b'/a'	V(Å^3)
FeO	DFT (this work)	-0.67	1.02	0.973	21.18
	DFT [59]	-0.48	1.025	0.975	20.9
	Exp. [15, 60, 62]	-0.62	1.023	0.991	20.0 - 20.3
CoO	DFT (this work)	0.89	0.984	0.978	19.61
	DFT [59]	0.80	0.976	0.985	19.8
	Exp. [14, 60]	0.3	0.988	0.999	19.3

III. RESULTS

A. Structural distortions

Below the Néel temperatures, the AF-II magnetic order breaks the cubic symmetry of the rocksalt structured TMOs. This results in a rhombohedral distortion $R\bar{3}m$ symmetry for MnO [7, 11, 12, 60] and NiO [10, 11, 61], and a further lowering of the symmetry to a monoclinic $C2/m$ structure is observed for FeO [15, 60, 62] and CoO [14, 60].

We create simulation cells with rhombohedral and mononclinic distortions and relax the TMO structures. Tables I and II compare the calculated rhombohedral and monoclinic distortions, respectively, with previous DFT calculations [59] and experimental measurements [7, 10–12, 14, 15, 60–62]. For all four TMOs, we find the same structural distortions as experimentally observed and with the structural parameters in close agreement with the previous DFT study and the measured values. The small differences between the previous and present DFT studies are likely due to differences in the computational parameters such as pseudopotential choices and k-point density.

We created supercells from these structures for slab calculations. The lattice parameters of the supercells can be calculated from the volume of the cubic supercell, V_{scell}, which is 32 times the volumes provided in tables I and II, and angle, α for the rhombohedral cell,

$$a = \sqrt[3]{\frac{V_{scell}}{\sqrt{1 + 2 \cdot \cos^3 \alpha - 3 \cdot \cos^2 \alpha}}} \quad (1)$$

For the monoclinic case, the lengths of the three lattice parameters is given by

$$a = \sqrt[3]{\frac{V_{scell}}{b/a \cdot c/a}} \quad (2)$$

B. Magnetic structure of bulk phases

To accurately describe the magnetic structure of the four TMOs, we relax their structure for non-spinpolarized (NM), ferromagnetic (FM), and antiferromagnetic type II ordering (AF-II) configurations. The AF-II configuration with the respective distorted structures results in the lowest energy for all four oxides, in agreement with the experimental observations that these oxides are antiferromagnetic insulators at low temperatures, validating the PBE+U approach for the low-temperature magnetic phases.

C. Disordered local moment paramagnetism

MnO, FeO, and CoO are paramagnetic at room temperature. Paramagnetic phases are frequently described using non-spinpolarized DFT. However, the NM configurations of all four oxides have 0.8 to 2.0 eV higher energies than the AF-II configuration, which is inconsistent with the observed Néel temperatures of the oxides. Furthermore, for MnO, CoO, and NiO the NM configuration results in a metallic electronic structure, in contrast to the experimentally measured large bandgaps [63–73]. This demonstrates that a non-spinpolarized solution does not well describe these TMOs in agreement with the recent DFT study by Trimarchi *et al.* [46]. Also, the ferromagnetic ordering also fail to capture the bandgaps for these oxides.

We test whether a disordered local moment state can more accurately describe the energetic stability and electronic structure of the paramagnetic phase compared to the NM configuration. We model the disordered local moments using special quasirandom structures (SQS) that are generated with the mcsqs code of the Alloy Theoretic Automated Toolkit [74]. Figure 3 illustrates the AF-II ordering and an SQS representation of the disordered local moments.

Among many possible SQS structures, we create seven different structures with the number of inequivalent pair and triplet clusters ranging from 7 to 40 in the 64 atom unit cell. We find that for a given TMO the energy and volume for five of the SQS structures are very similar and vary with a small standard deviation of 1, 2, 11, and 2 meV/atom for the energy and 0.02, 0.06, 0.03, and 0.03 Å^3/atom for the volume for MnO, FeO, CoO, and NiO, respectively. Two SQS configurations exhibit an energy 0.2 - 1.1 eV higher than the other five SQS configurations for all four TMOs. We observe that the five low-energy SQS structures also exhibit similar densities of states and bandgaps. In our following analysis, we consider the lowest energy SQS structure for each TMO that possess a net zero magnetic moment and displays a similar electronic structure as experimentally observed.

Table III compares the energies and bandgaps of the different magnetic configurations for each of the four oxides with experimental observations to validate the different magnetic descriptions. The SQS structures are only slightly higher in energy than the AF-II structures, but similar in terms of their electronic properties. The energy differences are consistent with the measured Néel temperatures, indicating that the local moment configuration more accurately describes the paramagnetic state in these four oxides. Also, the SQS structures exhibit

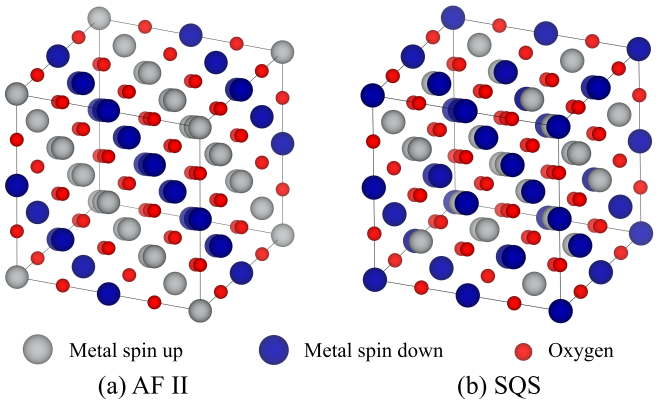

FIG. 3. The $2 \times 2 \times 2$ supercell of CoO with (a) antiferromagnetic type II ordering and (b) disordered spins using a special quasirandom structures.

TABLE III. Comparison of the energy, ΔE_{bulk} (calc.) in eV/atom, and electronic structure of the four TMO in the NM, AF-II, and SQS magnetic configurations with available experimental data. The energy, ΔE_{bulk}, is measured relative to the AF-II ground state configuration of the spins. The bandgaps, E_{gap} in eV, calculated with the PBE+U method slightly underestimate the experimental values. In addition, we show the calculates d-orbital splitting, ΔE_d in eV, and the used Hubbard-U parameter in eV for the TM d-electrons.

	MnO			**FeO**			**CoO**			**NiO**		
	NM	AF-II	SQS	NM	AF-II	SQS	NM	AF-II	SQS	NM	AF-II	SQS
ΔE_{bulk} (calc.)	2.02	0	0.005	1.01	0	0.009	0.79	0	0.074	1.16	0	0.012
E_{gap} (calc.)	0	1.8	0.9	2.8	1.8	1.8	0	2.3	1.6	0	3.5	2.3
E_{gap} (exp.)		3.6 - 3.8 [63]			2.4 [64]			2.5 [65], 2.6 [66]			3.7 [67], 4.0 [66]	
		3.9 [68], 4.1 [66]						3.6 [69], 5.4 [70]			4.0 [66], 4.3 [71]	
ΔE_d		3.8	2.8		2.8	3.2		2.4	1.8		3.8	2.8
U		3.9			5.3			3.32			6.2	

similar volumes with the volume of the AF-II structures, about 0.5% smaller than for the AF-II configurations for MnO, FeO, CoO and NiO.

D. Bulk electronic density of states and bandgaps

To confirm the importance of the local moments in the paramagnetic state and to validate our approach, we compare the prediction of the electronic bandgaps with experimental data for the four oxides. Fig. 4 shows the electronic spin density of states (DOS) projected on the s states of the cations and oxygen and the d states of the cations for the AF-II and SQS configurations of MnO, FeO, and CoO and NiO. For the AF-II configurations, Fig. 4a, we project the DOS onto the states of just one up-spin cation. The down spin cation exhibits an inverted DOS, keeping the overall electronic structure antiferromagnetic. In case of the SQS configurations, the projected DOS shown in Fig. 4(b) is the average over all the up spin atoms in the structure, accounting for the contribution of all up spin atoms in the SQS supercell.

For both the AF-II and the SQS configurations, we observe that the d-band splitting, *i.e.*, the gap in the DOS contributed only by the d states, is larger than the overall bandgap. The cation d states dominate the valence band maximum, and the transition metal s states comprise the conduction band minimum with a small but finite DOS. The DOS of the cation d bands are two orders of magnitude higher than of the s bands, with the oxygen p bands displaying an intermediate density of states. We note that the p-bands lie away from bandgap and do not provide additional information. With the increasing number of d electrons from Mn to Ni, the d-DOS increases as the added electrons occupy spin states following Hund's rule of multiplicity. **We observe significant difference in the density of states between the AF-II and the random local moment SQS configurations, even though the energy differences between the ordered and disordered states are quite small. First, the conduction band states that are dominated by the s orbitals significantly change and move into the bandgap region for almost all oxides. This reduces the bandgap but does not alter the ground state energy. Second, the peaks are broadened in the SQS configuration due to the increased spin disorder and corresponding small local structural distortions.**]

Next, we compare the electronic structure of the disordered local moment configurations with experimental observations. We focus in particular on the measured bandgap, the d-band splitting, and the small contribution of the s states to the DOS at the bottom of the conduction band. For MnO, the Mn d-band splitting is 3.8 eV in the AF-II configuration and 2.8 eV in the case of disordered local moments. The calculated d-band splitting agrees closely with the larger values of the measured bandgaps, ranging from 3.6 to 4.1 eV [63, 66, 68], which may be explained by the high DOS of the d states. **However, the cation s bands extend below the conduction band d states. The resulting low DOS tail of s bands reduces the bandgap, which is particularly profound in MnO and FeO.** A similar tail of low DOS at the conduction band minimum was experimentally observed [68].

For FeO, the bandgap is similar in both the AF-II and the disordered local moment configuration. The SQS configuration displays a set of peaks in the s-DOS at the bottom of the conduction band, which are not found in the AF-II configuration. For CoO, the d-band splitting is 2.4 and 1.8 eV for the AF II and SQS configurations, respectively, both of which are smaller than the experimental bandgap. We also find that the energy difference between the disordered local moment configuration and the AF-II ordering is larger for CoO compared to the other three TMOs, which invites further study on the contributions of local moments to the energy of the different TMOs.

NiO shows the largest d-band splitting in the four TMOs. The Néel temperature of NiO is 525 K. We also calculate and show the DOS of the SQS configuration of NiO. The s-states at the conduction band minimum lead

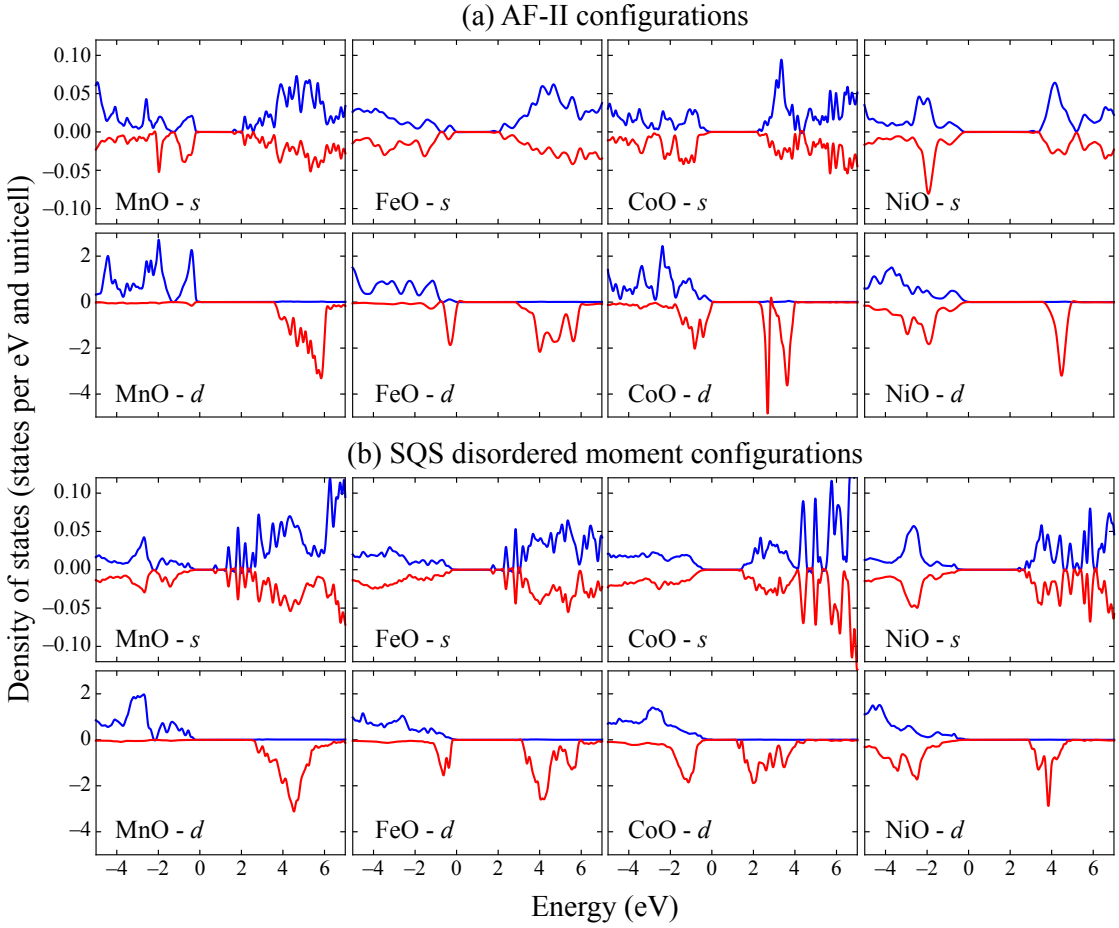

FIG. 4. The spin-density of states (DOS) projected onto the s and d orbitals for the (a) AF-II ordered and (b) disordered local moment (SQS) structures of MnO, FeO, CoO, and NiO. The s-orbital DOS contains contributions from both metal and oxygen atoms, whereas the d-orbital DOS consists of contributions from the TM atoms only. We show the DOS of only one TM atom (up spin) in case of AF-II structures, whereas, for the SQS structures, we average over all up-spin TM atoms. The plots show that the metal d-orbital exhibit a large band splitting and higher density of states compared to the s orbitals which extend into the bandgap region of the d orbitals.

to a bandgap of 3.5 eV which is close to the experimentally observed bandgap of 3.8 eV to 4.3 eV [67, 70, 71].

To summarize the results for the TMO bulk phases, we find that the magnetic ordering strongly affects their electronic structure [9] and breaks the cubic symmetry. The band gaps and features like the tails of s-orbital states near the conduction band minima in the density of states are similar to the results by Trimarchi *et al.* [46]. The small difference in these calculated properties are likely due to the choice of U-values, supercell sizes, and other calculation parameters. The agreement of our calculations with experiment demonstrate that modeling the paramagnetic phase by disordered local moments, represented by SQS configurations of the spins, provides an accurate description of energetic stability and electronic structure of the paramagnetic state.

E. Surface energies

We calculate the surface energies of the (100), (110), and (111) facets for the four oxides for the AF-II magnetic configuration for all four TMOs and for the disordered local moment configuration for MnO, FeO, and CoO to describe the room temperature paramagnetic phase. To elucidate the importance of the random local moments on the surface energy for the paramagnetic phase, we also consider the NM configuration for MnO and FeO. To estimate the effect of an aqueous environment on the surface energies, we also determine the surface energy using the continuum solvation model VASPsol [47, 48].

We construct slabs with varying thickness for the three facets from the bulk calculations of the four oxides using the MPInterfaces package [57]. As discussed in Sec. III B, the cubic symmetry is broken by the magnetic order of the rocksalt AF-II and SQS structures results in distor-

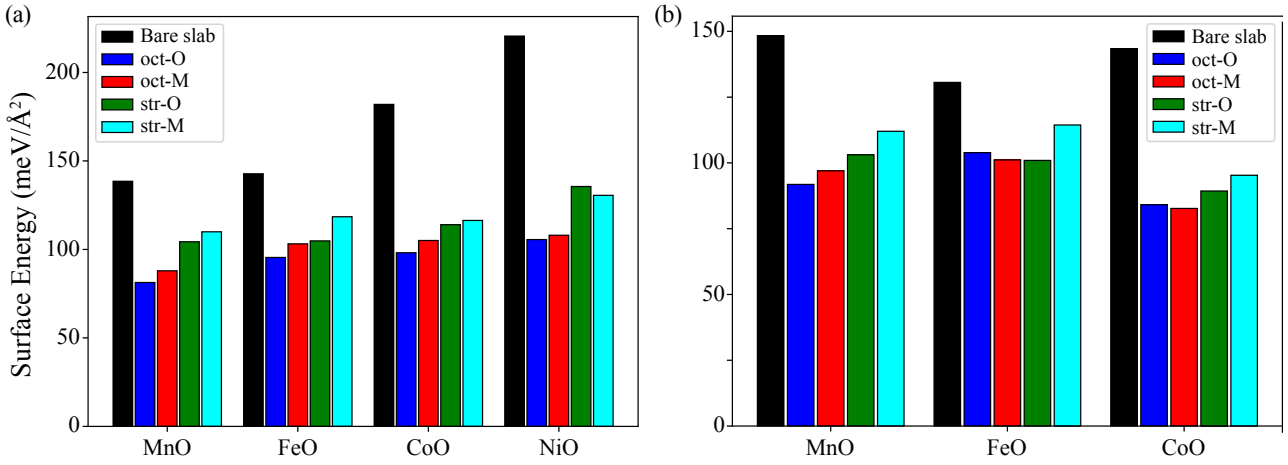

FIG. 5. Comparison of surface energies of the (111) reconstructions for MnO, FeO, CoO, and NiO with (a) AF-II ordering and (b) random local moment SQS configurations. Note that the SQS calculations are not performed on NiO because because it is antiferromagnetic at room temperature.

tions of the rocksalt cubic structure [59]. While the rhombohedral distortions in MnO and NiO due to the AF-II order are quite small, the monoclinic distortions in FeO and CoO are more significant. When neglecting the distortions, we find that a small residual strain for MnO and NiO, and a larger strain for FeO and CoO that results in inconsistent energies. Therefore, we include the monoclinic distortions in the FeO and CoO slabs and neglect the rhombohedral distortions in MnO and NiO. We find that neglecting the small rhombohedral distortions for MnO and NiO changes the surface energies by a negligible amount of less than 2 meV/Å^2.

The polar (111) surfaces of the rocksalt structure reconstruct and we determine the most stable reconstructions for each of the four oxide systems. Figure 5 compares the energies of the unreconstructed and reconstructed (111) surfaces of the AF-II and random local moment SQS configurations for the four oxides. The thickness of slabs for all reconstructions are maintained within a similar range for appropriate comparison. We observe that the octopolar reconstructed surfaces have lower surface energies than the stripes reconstruction and the bare slabs. The oxygen-terminated octopolar reconstruction is the most stable one for all AF-II structures in vacuum, whereas the metal-terminated octopolar reconstruction is the most stable one for the SQS structures of FeO and CoO. The energies of the reconstructions for FeO are all within a few meV, suggesting that the (111) FeO surface might undergo different reconstruction or disorder under different conditions. In contrast, the other oxides clearly prefer the octopolar reconstruction for the (111) surface.

To estimate the effect of an aqueous environment on the surface energies, we relax all slabs also using the continuum solvation model, VASPsol, with a relative permittivity of $\epsilon_r = 80$, representing water. The presence of the solvent reduces the energies of the slabs by a few meV and the stable reconstructions remained the same

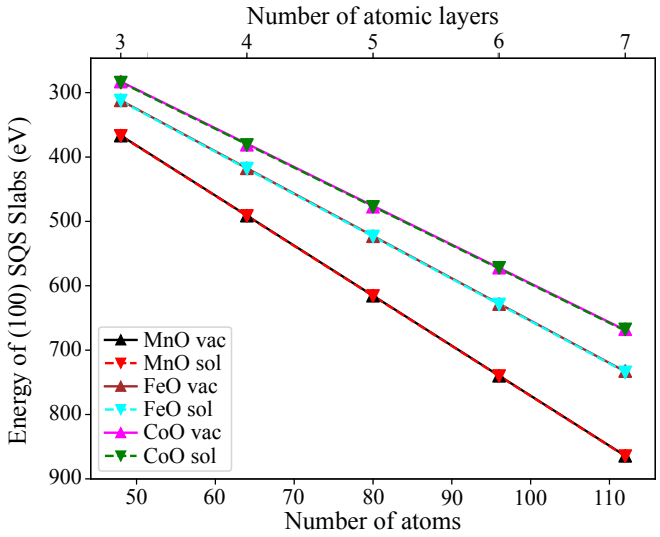

FIG. 6. The energies of the (100) slabs as a function of the number of atomic layers for the random local moment SQS configuration. The surface area of the slabs is maintained constant while increasing the number of atoms and atomic layers in the slab. The data from the calculations is fit using multivariate linear regressions of the energy. The solid and dashed lines correspond to the fits for the vacuum and solvent calculations, respectively.

for all systems as in vacuum except for AF-II CoO, where octopolar reconstruction with metal ends is lowest energy configuration in solvent medium, illustrating that the presence of solvent can modify which surface structures is most stable.

To extrapolate the surface energies to infinite slab thickness, we perform the surface energy calculations as a function of increasing slab thickness. For the random local moment configurations represented by the SQS structures, the surface spin configurations vary with slab

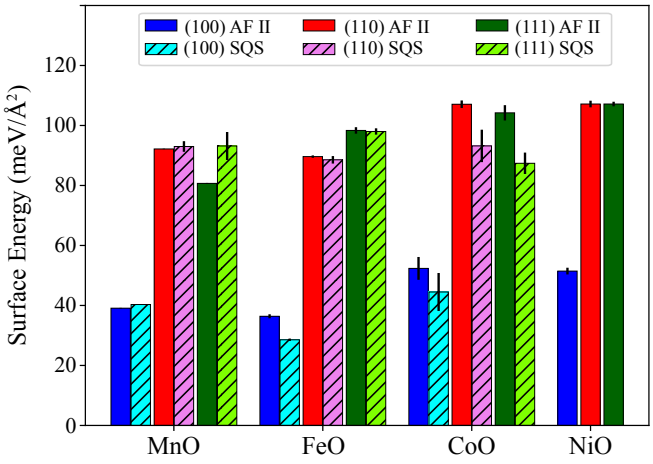

FIG. 7. Surface energies of the metal oxides extrapolated to infinite slab thickness for the antiferromagnetic and paramagnetic phases in the AF-II and SQS configurations, respectively. The solid bars represent the AF-II configurations and the striped bars the random-local moment configurations represented by the SQS structures. The error bars are also shown for surface energies of each facet. The surface energies of the (100) facets in all oxides is sufficiently low compared to the other facets, such that all the oxides form cubic nanocrystals.

thickness. Hence, in addition to correcting for the finite slab thickness, the extrapolation also effectively averages over the different surface spin configurations. We fit the total energy, E_{hkl} of the finite-thickness slabs to the function

$$E_{hkl} = N E_{\text{bulk}} + 2A_{hkl}\,\gamma_{hkl}, \tag{3}$$

where N is the number of atoms in the slab, E_{bulk} is the bulk energy, A_{hkl} the surface area, and γ_{hkl} the surface energy of the $\{hkl\}$ facet.

To obtain a single value for the bulk energy, E_{bulk}, from the data for all slabs of a given material, we perform a single multivariate least squares optimization using the SciPy [75] function scipy.optimize.minimize() to simultaneously fit the total energies of all the calculations, three facets – (100), (110), and (111) – in two different enviroments – vacuum and water – as a function of the number of atoms in the slab. We use squared weights to bias the fit of the energy towards thicker slabs, which are expected to have reduced interactions between their top and bottom surfaces. For each material, the fit results in the six surface energies for the three facets in each of the two environments, and a single bulk energy.

Figure 6 illustrates, as an example, the fit for the (100) surfaces of the SQS structures of MnO, FeO, and CoO. The results for the other facets look similar. The slopes of the lines in Fig. 6 indicate the bulk energy and the extrapolation to zero layers corresponds to the surface energy. The solid and dashed line correspond to the vacuum and solvent calculations, respectively. The presence of solvent only slightly reduces the surface energies.

Figure 7 compares the extrapolated surface energies of the four oxides for the AF-II and random local moment configurations, and Table IV provides the fitted surface energies and their uncertainties. We find that the (100) surface is generally the lowest energy facet. Several of the surface energies of MnO and FeO in the AF-II and disordered local moment configurations are nearly degenerate. However, the SQS configurations exhibit slightly higher surface energies for MnO and slightly lower ones for FeO. For CoO, the SQS configurations exhibit lower surface energies for all surfaces. The observed reduction in surface energy due to the loss of magnetic order increases from MnO to FeO to CoO, which corresponds to their increasing energy difference of the paramagnetic and AF-II configurations and Néel temperatures of T_N = 116 K, 198 K, and 291 K, respectively. The same trend is observed in the differences of the bulk energies due to transition from the AF-II to random ordering shown in Table III. We also calculated the standard deviation of the atomic displacement in the bulk supercells of the SQS configurations for each oxide. We find that the magnitude of the relaxations due to the magnetic disorder is largest in CoO, smallest in MnO, with FeO in between. So, as T_N increases, the oxide surfaces tend to relax more and further minimize their surface energy in the paramagnetic disordered local moment phase.

In addition, we calculate the standard deviation of the distribution of surface energies from each calculation of a facet to estimate the uncertainty of the surface energies, shown in Fig. 7. The surface energies from different calculations converge for FeO and NiO, represented with negligible error bars, whereas, the (111) surface energy of the SQS configuration of MnO and the surface energies of CoO show somewhat larger fluctuations. The SQS slabs of reconstructed (111) facet tend to settle in local minima resulting in the error. CoO slabs also exhibit the same problem.

To investigate the errors in CoO, we fitted the bulk energy for each facet separately and compared them for all materials. We find that the difference in the fitted bulk energies for CoO is large compared to negligible differences in other oxides. This suggests that the slab thickness is not sufficient for the middle layers to resemble bulk CoO. Although thicker slabs might provide better description of the CoO surfaces, it is challenging as the calculations become more expensive and tend to relax into local minima. The complex behavior of CoO compared to other oxides needs to be studied further.

The surface energies determine the equilibrium crystal shape. Using the Wulff construction implemented in the MPInterfaces python package, we find that the AF-II and paramagnetic disordered local moment phase exhibit a cubic equilibrium crystal shape for the four oxides in both the AF-II and paramagnetic phase in vacuum and solvent. Noteworthy, describing the paramagnetic phase of MnO using a non-spinpolarized calculation would lead to a significantly reduced ratio of the surface energies of (111) and (100) and an octahedral crystal shape. In an aqueous solvent, the high-energy (110) and (111) facets

TABLE IV. Fitted surface energies of all TMOs in AF-II and paramagnetic SQS phases. The corresponding errors (in parantheses) are the standard deviation of surface energies from calculations of different thickness for each facet. , $\Delta E_{\text{bulk}}^{\text{fit}}$, is the difference between the fitted bulk energies and the bulk energy calculated.

		$\Delta E_{\text{bulk}}^{\text{fit}}$	Surface energy (meV/Å^2)		
		(eV/atom)	(100)	(110)	(111)
MnO	AF-II	0.001	39.1 (0.1)	92.2 (0.1)	80.7 (0.2)
	SQS	-0.001	40.3 (0.1)	93.0 (1.8)	93.2 (4.7)
FeO	AF-II	0.003	36.4 (0.7)	89.6 (0.4)	98.3 (1.1)
	SQS	0.007	28.6 (0.4)	88.6 (1.2)	98.0 (1.1)
CoO	AF-II	-0.009	52.4 (3.8)	107.1 (1.3)	104.2 (2.6)
	SQS	-0.014	44.5 (6.3)	93.2 (5.4)	87.4 (3.6)
NiO	AF-II	-0.002	51.5 (1.1)	121.8 (1.1)	107.2 (0.8)

reduce their energies to a greater extent compared to the low energy (100) surface. However, the relative ratios of the surface energies do not change enough to lead to a change in crystal shape.

IV. CONCLUSION

In this study, we have calculated the bulk and surface properties of the four magnetic oxides, MnO, FeO, CoO, and NiO using the DFT+U approach. We consider the low-temperature antiferromagnetic type-II phases and the room temperature paramagnetic phases. We show that an accurate description of the energy and electronic structure of the paramagnetic phases requires a disordered local moment representation instead of a nonspinpolarized approach and use special quasirandom supercell structures for the paramagnetic phase.

The calculated electronic structure of the AF-II and paramagnetic structures are consistent with experimental data. The densities of states show a weak s-orbital contribution that extends below the d-dominated conduction band states, which are caused by the significant d-d splitting in these oxides. Our results are consistent with optical absorption measurements and indicate that the d-d splitting dominates the optical absorption. The low-intensity s-states are expected to lead to a weak signal in optical absorption measurements consistent with experimental observations.

Using our validated DFT approach, we calculate the (100), (110), and (111) surface energies of the AF-II and paramagnetic phase for each oxide. We show that the most stable reconstruction of the polar (111) surface is the octopolar reconstruction with oxygen and metal termination being nearly degenerate for all oxides. For the paramagnetic phase of FeO we find that the metal-terminated stripes reconstruction is similar in energy. Using a finite-size extrapolation, we obtain the surface energies of the oxides in vacuum and solvent. The final energies and error bars suggest that larger supercells with monoclinic distortions are important for FeO and CoO, whereas the small rhombohedral distortions for MnO and NiO do not have significant affect on their surface properties. On the downside, care should be taken to prevent relaxing to local minima.

The Wulff construction shows that all four oxides display a cubic equilibrium crystal shape. The presence of an aqueous solvent lowers the surface energies by different fractions for each facet, however, the shape of the nanocrystal remains cubic.

ACKNOWLEDGMENTS

This work was supported by the National Science Foundation under the under awards OAC-1740251 and DMR-1609306. This research used computational resources of the Texas Advanced Computing Center under Contract Number TG-DMR050028N and of the University of Florida Research Computing Center. Part of this research was performed while the authors were visiting the Institute for Pure and Applied Mathematics (IPAM), which is supported by the National Science Foundation.

[1] H. H. Kung, *Transition metal oxides: Surface chemistry and catalysis*, Vol. 45 (Elsevier, 1989).
[2] A. Nelson, K. E. Fritz, S. Honrao, R. G. Hennig, R. D. Robinson, and J. Suntivich, J. Mater. Chem. A **4**, 2842 (2016).
[3] E. Aytan, B. Debnath, F. Kargar, Y. Barlas, M. M. Lacerda, J. X. Li, R. K. Lake, J. Shi, and A. A. Balandin, Appl. Phys. Lett. **111**, 252402 (2017).
[4] P. L. S. G. Poizot, S. Laruelle, S. Grugeon, L. Dupont, and J. M. Tarascon, Nature **407**, 496 (2000).
[5] M. V. Reddy, G. V. Subba Rao, and B. V. R. Chowdari, Chem. Rev. **113**, 5364 (2013).
[6] Q. Liu, Q. Chen, Q. Zhang, Y. Xiao, X. Zhong, G. Dong, M.-P. Delplancke-Ogletree, H. Terryn, K. Baert, F. Reniers, and X. Diao, J. Mater. Chem. C **6**, 646 (2018).
[7] W. L. Roth, Phys. Rev. **110**, 1333 (1958).
[8] K. Terakura, A. R. Williams, T. Oguchi, and J. Kübler, Phys. Rev. Lett. **52**, 1830 (1984).
[9] K. Terakura, T. Oguchi, A. R. Williams, and J. Kübler, Phys. Rev. B **30**, 4734 (1984).
[10] G. A. Slack, J. Appl. Phys. **31**, 1571 (1960).
[11] A. K. Cheetham and D. A. O. Hope, Phys. Rev. B **27**, 6964 (1983).
[12] H. Shaked, J. Faber Jr, and R. L. Hitterman, Phys. Rev. B **38**, 11901 (1988).
[13] D. Herrmann-Ronzaud, P. Burlet, and J. Rossat-

Mignod, J. Phys. C: Solid State Phys. **11**, 2123 (1978).
[14] W. Jauch, M. Reehuis, H. J. Bleif, F. Kubanek, and P. Pattison, Phys. Rev. B **64**, 052102 (2001).
[15] H. Fjellvåg, B. C. Hauback, T. Vogt, and S. Stølen, Am. Mineral. **87**, 347 (2002).
[16] C. Kittel, *Introduction to solid state physics*, 8th ed. (Wiley, 2004).
[17] C. Noguera, J. Phys.: Cond. Mater. **12**, R367 (2000).
[18] G. Renaud, Surf. Sci. Rep. **32**, 5 (1998).
[19] C. Franchini, V. Bayer, R. Podloucky, G. Parteder, S. Surnev, and F. P. Netzer, Phys. Rev. B **73**, 155402 (2006).
[20] K. Koike and T. Furukawa, Phys. Rev. Lett. **77**, 3921 (1996).
[21] W. Ranke, M. Ritter, and W. Weiss, Phys. Rev. B **60**, 1527 (1999).
[22] Y. Joseph, W. Ranke, and W. Weiss, J. Phys. Chem. B **104**, 3224 (2000).
[23] S. Shaikhutdinov, M. Ritter, and W. Weiss, Phys. Rev. B **62**, 7535 (2000).
[24] K. Mori, M. Yamazaki, T. Hiraki, H. Matsuyama, and K. Koike, Phys. Rev. B **72**, 014418 (2005).
[25] D. Cappus, M. Haßel, E. Neuhaus, M. Heber, F. Rohr, and H.-J. Freund, Surf. Sci. **337**, 268 (1995).
[26] M. Hassel and H.-J. Freund, Surf. Sci. **325**, 163 (1995).
[27] C. Mocuta, A. Barbier, and G. Renaud, Appl. Surf. Sci. **162**, 56 (2000).
[28] D. Cappus, C. Xu, D. Ehrlich, B. Dillmann, C. A. Ventrice, K. Al Shamery, H. Kuhlenbeck, and H.-J. Freund, Chem. Phys. **177**, 533 (1993).
[29] O. L. Warren and P. A. Thiel, J. Chem. Phys. **100**, 659 (1994).
[30] F. Rohr, K. Wirth, J. Libuda, D. Cappus, M. Bäumer, and H.-J. Freund, Surf. Sci. **315**, L977 (1994).
[31] H. Hannemann, C. A. Ventrice, T. Bertrams, A. Brodde, and H. Neddermeyer, Phys. Stat. Sol. (a) **146**, 289 (1994).
[32] C. A. Ventrice Jr, T. Bertrams, H. Hannemann, A. Brodde, and H. Neddermeyer, Phys. Rev. B **49**, 5773 (1994).
[33] P. M. Oliver, G. W. Watson, and S. C. Parker, Phys. Rev. B **52**, 5323 (1995).
[34] A. Barbier and G. Renaud, Surf. Sci. **392**, L15 (1997).
[35] A. Barbier, C. Mocuta, H. Kuhlenbeck, K. F. Peters, B. Richter, and G. Renaud, Phys. Rev. Lett. **84**, 2897 (2000).
[36] A. Barbier, C. Mocuta, and G. Renaud, Phys. Rev. B **62**, 16056 (2000).
[37] O. Bengone, M. Alouani, J. Hugel, and P. Blöchl, Comput. Mater. Sci. **24**, 192 (2002).
[38] A. Wander, I. J. Bush, and N. M. Harrison, Phys. Rev. B **68**, 233405 (2003).
[39] F. Finocchi, A. Barbier, J. Jupille, and C. Noguera, Phys. Rev. Lett. **92**, 136101 (2004).
[40] A. Wander, F. Schedin, P. Steadman, A. Norris, R. McGrath, T. S. Turner, G. Thornton, and N. M. Harrison, Phys. Rev. Lett. **86**, 3811 (2001).
[41] N. G. Condon, P. W. Murray, F. M. Leibsle, G. Thornton, A. R. Lennie, and D. J. Vaughan, Surf. Sci. **310**, L609 (1994).
[42] G. H. Vurens, M. Salmeron, and G. A. Somorjai, Surf. Sci. **201**, 129 (1988).
[43] F. Allegretti, C. Franchini, V. Bayer, M. Leitner, G. Parteder, B. Xu, A. Fleming, M. G. Ramsey, R. Podloucky, S. Surnev, and F. P. Netzer, Phys. Rev. B **75**, 224120 (2007).
[44] G. A. Rizzi, R. Zanoni, S. Di Siro, L. Perriello, and G. Granozzi, Surf. Sci. **462**, 187 (2000).
[45] G. A. Rizzi, M. Petukhov, M. Sambi, R. Zanoni, L. Perriello, and G. Granozzi, Surf. Sci. **482**, 1474 (2001).
[46] G. Trimarchi, Z. Wang, and A. Zunger, Phys. Rev. B **97**, 035107 (2018).
[47] K. Mathew, R. Sundararaman, K. Letchworth-Weaver, T. Arias, and R. G. Hennig, J. Chem. Phys. **140**, 084106 (2014).
[48] K. Mathew, V. S. C. Kolluru, S. Mula, and R. G. Steinmann, Stephan N.and Hennig, J. Chem. Phys. **151**, 234101 (2019).
[49] G. Kresse and J. Furthmüller, Comput. Mater. Sci. **6**, 15 (1996).
[50] P. E. Blöchl, Phys. Rev. B **50**, 17953 (1994).
[51] G. Kresse and D. Joubert, Phys. Rev. B **59**, 1758 (1999).
[52] J. P. Perdew, K. Burke, and M. Ernzerhof, Phys. Rev. Lett. **77**, 3865 (1996).
[53] A. Jain, S. P. Ong, G. Hautier, W. Chen, W. D. Richards, S. Dacek, S. Cholia, D. Gunter, D. Skinner, G. Ceder, and K. a. Persson, APL Mater. **1**, 011002 (2013).
[54] A. Jain, G. Hautier, C. J. Moore, S. P. Ong, C. C. Fischer, T. Mueller, K. A. Persson, and G. Ceder, Comput. Mat. Sci. **50**, 2295 (2011).
[55] A. Jain, G. Hautier, S. P. Ong, C. J. Moore, C. C. Fischer, K. A. Persson, and G. Ceder, Phys. Rev. B **84**, 045115 (2011).
[56] T. M. Schuler, D. L. Ederer, S. Itza-Ortiz, G. T. Woods, T. A. Callcott, and J. C. Woicik, Phy. Rev. B **71**, 115113 (2005).
[57] K. Mathew, A. K. Singh, J. J. Gabriel, K. Choudhary, S. B. Sinnott, A. V. Davydov, F. Tavazza, and R. G. Hennig, Comput. Mater. Sci. **122**, 183 (2016).
[58] P. W. Tasker, J. Phys. C: Solid State Phys. **12**, 4977 (1979).
[59] A. Schrön, C. Rödl, and F. Bechstedt, Phys. Rev. B **86**, 115134 (2012).
[60] Y. Sumino, M. Kumazawa, O. Nishizawa, and W. Pluschkell, J. Phys. Earth **28**, 475 (1980).
[61] Y. Noguchi, M. Uchino, H. Hikosaka, T. Atou, K. Kusaba, K. Fukuoka, T. Mashimo, and Y. Syono, J. Phys. Chem. Solids **60**, 509 (1999).
[62] J. Zhang, Phys. Rev. Lett. **84**, 507 (2000).
[63] R. N. Iskenderov, I. A. Drabkin, L. T. Emelyanova, and Y. M. Ksendzov, Sov. Phys. Solid State **10**, 2031 (1969).
[64] H. K. Bowen, D. Adler, and B. H. Auker, J. of Sol. State Chem. **12**, 355 (1975).
[65] J. van Elp, J. L. Wieland, H. Eskes, P. Kuiper, G. A. Sawatzky, F. M. F. de Groot, and T. S. Turner, Phys. Rev. B **44**, 6090 (1991).
[66] E. Z. Kurmaev, R. G. Wilks, A. Moewes, L. D. Finkelstein, S. N. Shamin, and J. Kuneš, Phys. Rev. B **77**, 165127 (2008).
[67] R. J. Powell and W. E. Spicer, Phys. Rev. B **2**, 2182 (1970).
[68] J. van Elp, R. H. Potze, H. Eskes, R. Berger, and G. A. Sawatzky, Phys. Rev. B **44**, 1530 (1991).
[69] M. Gvishi and D. S. Tannhauser, J. Phys. Chem. Solids **33**, 893 (1972).
[70] T. D. Kang, H. S. Lee, and H. Lee, J. Korean Phys. Soc. **50**, 632 (2007).
[71] G. A. Sawatzky and J. W. Allen, Phys. Rev. Lett. **53**,

2339 (1984).
[72] G. W. Pratt Jr and R. Coelho, Phys. Rev. **116**, 281 (1959).
[73] D. R. Huffman, R. L. Wild, and M. Shinmei, J. Chem. Phys. **50**, 4092 (1969).
[74] A. Van de Walle, P. Tiwary, M. De Jong, D. L. Olmsted, M. Asta, A. Dick, D. Shin, Y. Wang, L.-Q. Chen, and Z.-K. Liu, Calphad **42**, 13 (2013).
[75] E. Jones, T. Oliphant, P. Peterson, *et al.*, "SciPy: Open source scientific tools for Python," (2001), [Online; accessed July 12, 2019].